

Scanning X-Ray Diffraction Microscopy for Diamond Quantum Sensing

Mason C. Marshall^{1,2,3,*} David F. Phillips² Matthew J. Turner^{3,4,5} Mark J. H. Ku^{3,6,7} Tao Zhou,⁸ Nazar Deegan^{9,10} F. Joseph Heremans,^{9,10,11} Martin V. Holt,⁸ and Ronald L. Walsworth^{1,2,3,12,†}

¹*Department of Electrical and Computer Engineering, University of Maryland, College Park, Maryland 20742, USA*

²*Center for Astrophysics | Harvard & Smithsonian, Cambridge, Massachusetts 02138, USA*

³*Quantum Technology Center, University of Maryland, College Park, Maryland 20742, USA*

⁴*Department of Physics, Harvard University, Cambridge, Massachusetts 02138, USA*

⁵*Center for Brain Science, Harvard University, Cambridge, Massachusetts 02138, USA*

⁶*Department of Physics and Astronomy, University of Delaware, Newark, Delaware 19716, USA*

⁷*Department of Materials Science and Engineering, University of Delaware, Newark, Delaware 19716, USA*

⁸*Center for Nanoscale Materials, Argonne National Laboratory, Lemont, Illinois 60439, USA*

⁹*Center for Molecular Engineering, Argonne National Laboratory, Lemont, Illinois 60439, USA*

¹⁰*Materials Science Division, Argonne National Laboratory, Lemont, Illinois 60439, USA*

¹¹*Pritzker School of Molecular Engineering, University of Chicago, Chicago, Illinois 60637, USA*

¹²*Department of Physics, University of Maryland, College Park, Maryland 20742, USA*

 (Received 15 March 2021; revised 13 August 2021; accepted 1 October 2021; published 16 November 2021)

An understanding of nano- and microscale crystal strain in chemical-vapor-deposition diamond is crucial to the advancement of diamond quantum technologies. In particular, the presence of such strain and its characterization presents a challenge to diamond-based quantum sensing and information applications—as well as for future dark-matter detectors, where the directional information about incoming particles is encoded in crystal strain. Here, we exploit nanofocused scanning x-ray diffraction microscopy to quantitatively measure crystal deformation from defects in diamond with high spatial and strain resolution. The combination of information from multiple Bragg angles allows stereoscopic three-dimensional modeling of strain-feature geometry; the diffraction results are validated via comparison to optical measurements of the strain tensor based on spin-state-dependent spectroscopy of ensembles of nitrogen-vacancy centers in the diamond. Our results demonstrate both strain and spatial resolution sufficient for directional detection of dark matter via x-ray measurement of crystal strain and provide a promising tool for diamond growth analysis and improvement of defect-based sensing.

DOI: [10.1103/PhysRevApplied.16.054032](https://doi.org/10.1103/PhysRevApplied.16.054032)

I. INTRODUCTION

Recently, quantum defects in diamond have emerged as a popular and growing platform for a variety of sensing applications [1–5]. While defect-ensemble-based sensing can achieve extremely high spatial resolution and sensitivity, these capabilities are subject to the homogeneity and quality of the host diamond [6,7]. Intrinsic strain in diamond limits many defect-based sensing applications; understanding and optimizing the local crystallographic environment of the defect is therefore a major effort in the quantum sensing and diamond growth communities

[6–8]. In particular, strain features with spatial structure near or below the visible-light diffraction limit are difficult to characterize via existing techniques such as optical birefringence [9] or nitrogen-vacancy (N-V) center spectroscopy [6,10,11]. However, such strain features negatively impact sensing applications by broadening quantum defect spin-transition line widths, thereby limiting their overall sensitivity to electromagnetic fields, temperature, and other phenomena [6]. Additionally, the boundaries of crystallographic strain defects act as charge traps [12], which may have deleterious effects on sensing via reduced spin coherence [13,14]. These issues are compounded by the need for fabricated optical microstructures and nanophotonic features for quantum information processing using N-V centers and other defects in diamond [15,16], which result in large strain over submicron

*Current address: Time and Frequency Division, NIST Boulder, Boulder, Colorado 80305, USA. mason.marshall@nist.gov

†walsworth@umd.edu

length scales [17]. A technique capable of characterizing short-length strain is necessary to better understand the interplay between local strain features and quantum point-defect sensors.

Strain sensing below the optical diffraction limit is also a crucial element of a proposed dark-matter (DM) detector in diamond capable of sensing the direction of incident particles [18]. Diamond is a promising target material for future detectors aimed at weakly interacting massive particles (WIMPs) and similar DM candidates [19]. Lasting crystal damage from WIMP collisions would act as a memory for the direction of the incoming particle and would be read out via a multistep detection process outlined in Sec. V. This directional information would enable discrimination from background solar and other neutrinos expected to limit the next generation of WIMP searches [20,21]. The demonstration of sensitive high-spatial-resolution strain measurement in diamond is an important step toward such a detector [22].

All of the applications highlighted here would also benefit from an understanding of the three-dimensional topology of strain features. Currently, a variety of techniques are used to produce low strain in quantum defect-hosting diamonds, including substrate surface treatment before chemical vapor deposition (CVD) and the annealing of CVD layers [7,8]. An understanding of the three-dimensional topology of the remaining strain features, and their evolution under such processes, could help optimize diamond growth and thus improve sensing performance. Finally, a three-dimensional measurement would also provide a fuller understanding of the strain around and within fabricated microstructures and allow prediction and mitigation of their effect on nearby defects.

In this paper, we demonstrate submicron and three-dimensional measurements of diamond strain with scanning x-ray diffraction microscopy (SXDM). Using the Hard X-ray Nanoprobe (HXN) at the Advanced Photon Source at Argonne National Laboratory [23]—illustrated schematically in Fig. 1(a)—we measure strain features on two diamond samples with high spatial resolution. To demonstrate sensitivity to spatially small features, we use a diamond produced by high-pressure high-temperature (HPHT) synthesis and exhibiting low strain at large length scales. Measurements on this sample demonstrate the resolution required to characterize local strain environments for single-defect quantum sensing and information applications, as well as to measure crystal-damage tracks for a WIMP search (as discussed in Sec. V).

To demonstrate that SXDM can obtain useful and otherwise inaccessible information in real-world quantum sensing conditions, without diamonds specifically engineered or selected for the purpose, we use a second diamond sample that is grown by CVD for N-V quantum sensing (for additional details about both samples, see Sec. A of the Supplemental Material [24]). On this sample, we measure

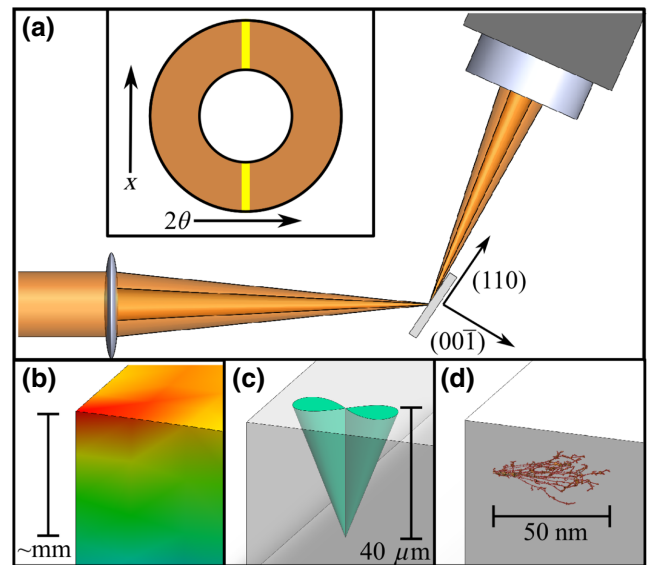


FIG. 1. (a) An illustration of scanning x-ray diffraction microscopy (SXDM). A monochromatic beam of hard x rays (here, 11.2 keV) is focused to a 25-nm spot at the diamond sample surface. The x rays undergo Bragg diffraction and are collected by a pixelated detector. The beam is scanned across the sample surface and a diffraction pattern is collected at each position. The inset shows a simplified schematic of the beam profile (orange ring). The yellow bar illustrates a simple diffraction pattern, as would be imaged from a perfect bulk crystal. Crystal strain shifts the Bragg angle θ , moving the diffraction pattern along the detector 2θ axis. (b)–(d) Illustrations of different crystal-strain features discussed in this work. (b) Macroscopic strain gradients arise across the diamond; for example, due to cleavage of a diamond into segments. (c) Dislocation features incorporated during CVD-diamond sample growth may create regions of strained crystal. (d) Microscopic damage to the diamond crystal—such as nuclear recoils following a WIMP or neutrino impact—leave characteristic strain signatures associated with displaced carbon nuclei in the lattice.

the three-dimensional spatial structure of larger strain features persisting throughout a 40- μm N-V-enriched overgrowth layer; high-resolution measurement of such deep defects is uniquely possible with SXDM, because of the deep penetration of the focused x-ray beam into the diamond. The multilayered structure of this diamond, with strain and impurity content variations within and between layers, yields a complex diffraction profile that is not well described by straightforward models. We therefore demonstrate a background-subtraction technique that enables quantitative measurement of small highly strained volumes occupying a subset of the beam-diamond interaction length. By combining SXDM measurements at different Bragg conditions and comparing the results to N-V spin-spectroscopic strain measurements, we demonstrate that SXDM successfully probes the internal three-dimensional

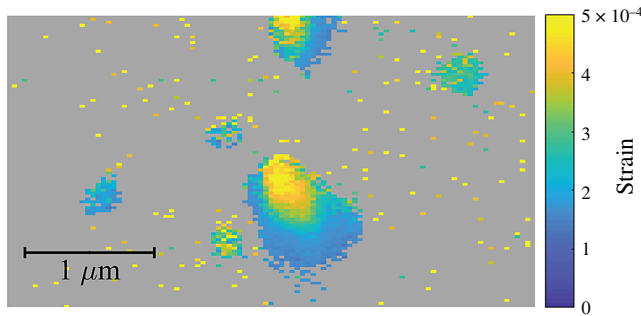


FIG. 2. Local strain features measured using SXDM on an HPHT diamond sample with a 22-nm scan step. Features are observed on length scales similar to the predicted strain from particle-induced crystal damage [18,22] (see Sec. V). These data are acquired via $(\bar{1}13)$ diffraction; for details of the analysis method, see the text.

structure of strain features that limit $N-V$ quantum imaging applications [6]. Finally, we characterize both the strain sensitivity and the prevalence of preexisting strain features in the CVD diamond as compared to requirements for the proposed WIMP detector [22], demonstrating a viable path to directional DM detection.

II. SCANNING X-RAY STRAIN MEASUREMENTS IN DIAMOND

The HXN focuses a bright monochromatic beam of x rays to a 10–25-nm spot and scans it across a sample held at a Bragg angle [25,26]. A two-dimensional photon-counting pixel detector records a diffraction pattern for each scan point. This pattern encodes the local crystal structure, including its spacing and orientation as well as its local impurity content [27]. When the beam passes through regions with differing crystal structure—such as the substrate and overgrowth layer of the CVD diamond—the resulting diffraction pattern will include contributions from each such region. Comparing diffraction patterns from nearby beam positions reveals differences in strain over short length scales. Figure 2 shows a map of local strain features in a region of the HPHT diamond obtained via such a comparison, illustrating the spatial resolution and sensitivity of SXDM on diamond. The approximately 100-nm length scale of the features observed here is comparable to that expected from a particle-induced damage track, as discussed in Sec. V. To extract the strain in these features, we use a background-subtraction technique developed to account for the complex diffraction pattern arising from the multilayered structure of the CVD diamond (see details below).

While the HPHT diamond mapped in Fig. 2 has a relatively homogeneous crystal structure, the CVD diamond includes several distinct volumes, schematically illustrated in Fig. 3(a). The uppermost $N-V$ -enriched overgrowth

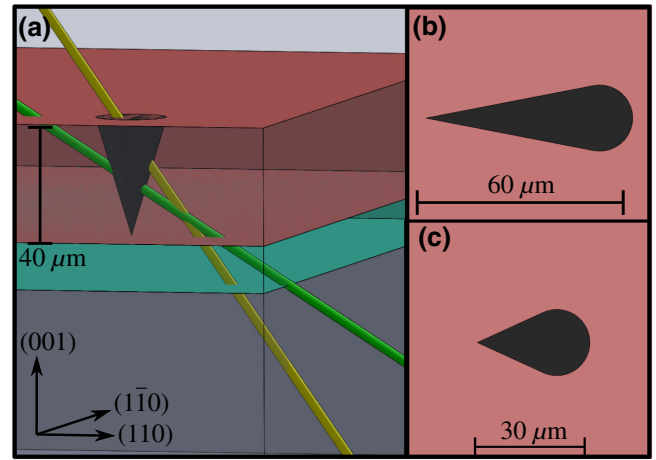


FIG. 3. (a) A schematic for Hard X-ray Nanoprobe (HXN) interrogation of the (113) and $(\bar{1}13)$ crystal planes on the CVD quantum sensing diamond. The green beam addresses the (113) plane, while the yellow beam addresses $(\bar{1}13)$. Layers with different lattice spacings and orientations diffract x rays within the beam differently, creating the diffraction pattern of Fig. 4(a). Schematically represented diamond components: the high-purity CVD substrate (gray), the polishing-damage layer at the substrate surface (green), and the $N-V$ -doped CVD overgrowth layer (red), which contains strained growth-defect features (black). (b),(c) Schematics of a strained growth-defect feature as projected onto the surface by scans addressing the (b) (113) and (c) $(\bar{1}13)$ crystal planes.

layer of the CVD diamond hosts crystal growth defects, which nucleate at imperfections on the substrate surface and exhibit large strains relative to the surrounding diamond. The substrate-layer interface features subsurface damage and a broad strain distribution due to mechanical polishing before CVD overgrowth [7]. Finally, the substrate is a 500- μm -thick high-purity diamond plate.

As the beam is scanned in two dimensions across the diamond surface, strain features at different depths in the crystal are therefore projected at an angle determined by the Bragg condition [as illustrated in Figs. 3(b) and 3(c)]. We use two distinct Bragg angles to image the CVD diamond, giving diffraction from the crystal planes with Miller indices (113) and $(\bar{1}13)$; combining the information from two projections allows us to constrain the three-dimensional structure of features in the sample.

The lattice spacing and crystal orientation vary through the diamond volume due to defect-induced strain, the impurity content, and mechanical processing damage. The diffraction pattern combines the contributions from all of these independent spatially varying effects. An example diffraction pattern acquired from the CVD sample is shown in Fig. 4(a). The diffraction pattern from an ideal unstrained 40- μm -thick diamond would appear as a single column of detector pixels in Fig. 4(a) [28,29]; the broad

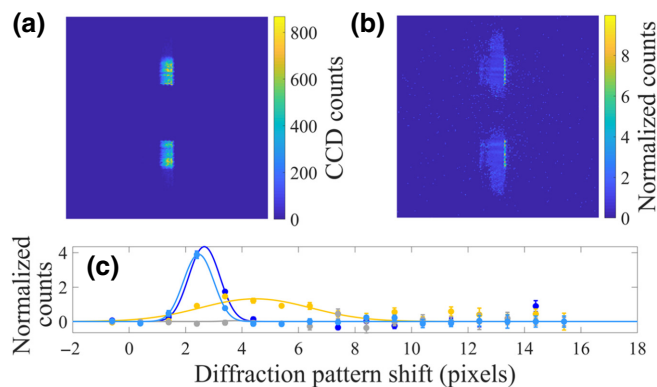


FIG. 4. (a) The diffraction pattern in the CVD-diamond sample measured at a single x-ray beam position, which includes contributions from multiple layers of the diamond as sketched in Fig. 3. (b) The diffraction pattern of (a) after dividing by the local host-crystal diffraction profile (for details, see Sec. C of the Supplemental Material [24]). This ratio emphasizes the contribution from sharp small-length-scale strain features such as crystal growth defects or recoil-induced damage. Each column of pixels in (b) is summed, yielding a one-dimensional diffraction curve, four of which are shown in (c). Each diffraction curve is fitted to a Gaussian line shape to extract a centroid and line width. The centroid position gives the mean strain in the feature, while the line width depends on the thickness of the feature along the beam path. The line colors are chosen to approximately match the strain scale of Fig. 5.

peak observed here arises from multiple complicating factors, including a variety of strain states among the layers as well as interactions at the layer interfaces.

The creation of a full analytical model of the diffraction pattern from such a sample requires detailed microscopic models for vacancy and impurity incorporation during the different CVD growth steps, for polishing damage at the substrate surface, and for crystal structure and x-ray diffraction behavior at the substrate-overgrowth interface. The development of such models is challenging because of the complexity of the stochastic processes involved, as well as the proprietary nature of diamond growth parameters. Instead, we analyze local strain features in the overgrowth layer, independent of the complex but slowly spatially varying overall line shape of the diffraction pattern associated with the layered diamond structure. Specifically, we focus on micrometer-to-nanometer-scale volumes strained relative to the surrounding crystal. These features are uniquely accessible through SXDM, and their interrogation is most relevant to both quantum sensor coherence properties and dark-matter detection applications. Two such features are schematically illustrated in Fig. 1: the clover-shaped dislocation feature of Fig. 1(c) and the nuclear recoil track of Fig. 1(d). Conversely, the strain gradient of Fig. 1(b) would contribute to the slowly varying overall line shape of the diffraction pattern and thus would not be highlighted in our analysis; strain over

these larger length scales can be more easily measured by other methods (see Sec. IV). While the HPHT diamond mapped in Fig. 2 has a more homogeneous crystal structure—lacking, for example, the N-V-enriched overgrowth layer of the CVD diamond—it still includes large-scale slowly varying strain effects due to mechanical polishing and a high nitrogen-impurity content. We therefore apply the same analysis to both diamonds.

The slowly varying overall line shape contains crystal structure and diffraction information about the surrounding diamond; to isolate and quantitatively analyze short-length strain features, we treat this line shape as a background and subtract it using a technique illustrated in Figs. 4(b) and 4(c). First, we construct a local host-crystal diffraction profile, by averaging diffraction patterns from nearby positions where the x-ray beam does not intersect strain features (for details on how this profile is constructed, see Sec. C of the Supplemental Material [24]). We then divide the measured diffraction pattern pixel by pixel with the host-crystal diffraction profile. This deemphasizes the slowly varying overall line shape and highlights the diffraction contribution from local strain features, resulting in a “reduced diffraction pattern,” as shown in Fig. 4(b). Crystal strain changes the Bragg angle θ , which shifts the diffraction pattern along the 2θ axis of the detector (chosen to lie in plane with the Bragg angle). We therefore sum each column of the reduced diffraction pattern to create a diffraction curve, as shown in Fig. 4(c). Finally, we fit these curves to a Gaussian line shape and extract the centroid position. (We choose a Gaussian because the spread of local impurity concentrations and strains within the beam spot should be approximately normally distributed.)

These measurements are sensitive to changes in both spacing and orientation of the diffracting crystal planes; sensitivity to both of these effects is valuable, as both types of lattice distortion affect defect-based sensing and both are expected to occur in a particle track. A comparison of the results obtained from two Bragg angles, combined with information from the two-dimensional shape of the diffraction pattern, constrains (but does not completely determine) the contributions of these effects (for this analysis, see Sec. B of the Supplemental Material [24]). To evaluate the sensitivity of this measurement and to quantify the amount of lattice distortion observed in our sample, we analyze the data in the case of uniform lattice orientation, where the signal arises entirely from strain-induced changes in the lattice spacing. Figure 5 demonstrates the results of this analysis.

To convert from the centroid position of the reduced line shape to strain (under this uniform-orientation condition), we generate calibration curves calculated using kinematic diffraction theory for a multilayered diamond structure [28,30] (for details on the generation of these curves, see Sec. D of the Supplemental Material [24]). Our samples are thick enough for dynamical diffraction effects

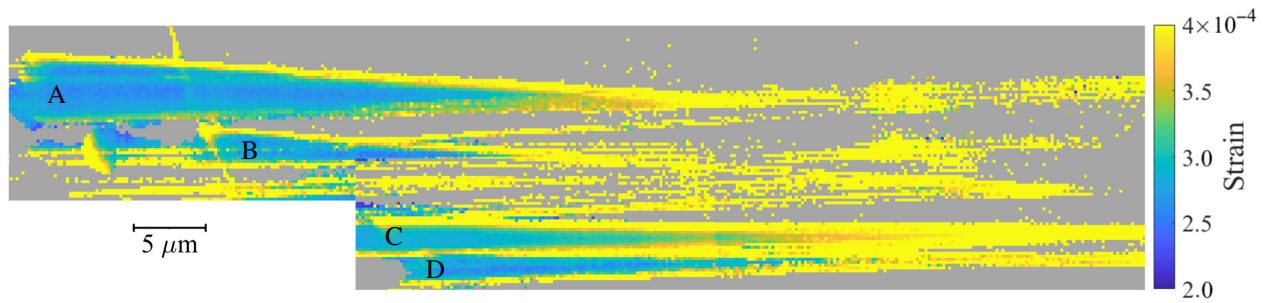


FIG. 5. A spatial map of the strain due to crystal dislocation features in one region of the CVD quantum sensing diamond, as measured with (113) diffraction. The gray color indicates x-ray beam positions that do not intersect a strain feature, as identified via a threshold on the amplitude of the background-subtracted diffraction curve [illustrated in Fig. 4(c)]. The four most prominent features are labeled A–D to simplify discussion in the main text. The same region and features are also measured with $(\bar{1}\bar{1}3)$ diffraction; for results, see Sec. G of the Supplemental Material [24]. The color-scale limits are chosen for legibility of internal strain within features, rather than enforced by the measurement. Note that the spatial resolution of this scan is set by the scanning step size of 200 nm, chosen to enable measurement of deep strain features over a relatively large field of view; the strain map shown here represents approximately 13 h of continuous data acquisition.

to manifest [29,31] but the resultant uncertainty in measured strain is small compared to other sources (for details, see Sec. F of the Supplemental Material [24]).

The width of the diffraction peak due to the surrounding crystal and substrate, together with the background-subtraction technique, impose a minimum detectable strain threshold on our measurements of local strain features. Background subtraction allows us to quantitatively investigate strain features in the top CVD layer, despite the presence of a broad and spatially inhomogeneous strain distribution in the surrounding crystal. However, background subtraction also suppresses features with diffraction peaks which are insufficiently shifted from the host-crystal diffraction profile. To be detectable with low uncertainty, a feature must have enough strain for its diffraction peak to be shifted out of the slowly varying overall diffraction profile. The actual minimum threshold depends on the line width of the host-crystal diffraction peak; in the CVD sample, it is approximately 1.5 detector pixels (for further details, see Sec. H of the Supplemental Material [24]). This leads to a minimum measurable compressive strain of approximately 1.6×10^{-4} .

Figure 5 shows a map of strain features in one region of the CVD diamond, as projected onto the (113) crystal axis. Each x-ray beam position is categorized, based on whether the amplitude of the reduced diffraction curve is greater than a threshold, as either part of a strain feature or as only containing the host crystal. Points where the beam does not intersect a strain feature are grayed out in Fig. 5; for strain-feature points, the calibrated strain is plotted at each beam position. The strain magnitude is determined from the centroid of the diffraction curve fit and the calibration curves. Four extended growth defects are clearly identifiable as blue regions labeled A–D in this map, with internal strains (in the uniformly oriented case) of $2.5 - 3 \times 10^{-4}$. We note that lattice distortion

in the features is high at the edges, while feature centers exhibit a smoothly varying structure. This ability to resolve differences in deformation within a growth defect demonstrates the power of SXDM with appropriate background subtraction to investigate crystal growth and defect incorporation.

In addition to these four extended defect regions, we also measure several thin, apparently linear high-distortion features; these are most likely the edges of extended defect regions exhibiting strain in a direction to which we are less sensitive. Bragg diffraction measures changes in the spacing between crystallographic planes—in other words, the projection of strain onto the axis of diffraction. For strain within growth features in diamond, the Burgers vector—the direction of the crystal-lattice distortion—generally points along one of the (110) family of crystal axes [32,33]. Unit vectors for axes in this family can have dot products of 0.9, 0.4, or 0 with the (113) and $(\bar{1}\bar{1}3)$ mirror planes used in our measurements. For example, if a feature has an average Burgers vector of (101), a (113) diffraction measurement would yield 0.9 times its nominal strain, while a measurement with $(\bar{1}\bar{1}3)$ diffraction would only yield 0.4 times the nominal strain. Comparing the projection onto different crystal planes thus allows us to constrain the average Burgers vector within particular strain features.

For features in certain projections, we may only detect the high-strain edges, while the strain in their central regions would be below this threshold. For example, features A and C of Fig. 5 have the same strain projection when measured with both $(\bar{1}\bar{1}3)$ and (113) diffraction. Therefore, assuming uniform lattice orientation as discussed above, their average Burgers vectors are likely along (011). Conversely, only the edges of features B and D are measurable using $(\bar{1}\bar{1}3)$ diffraction, meaning that their average Burgers vectors likely lie along (101) (again,

in the uniform-orientation case). The “rodlike” features observed in both diffraction angles are likely of similar origin, representing the high-strain edges of dislocation features with small projections onto both of our diffracting planes, having Burgers vectors mostly along the $(0\bar{1}1)$, (110) , or $(\bar{1}10)$ axes. The measured strain at the centers of features A–D in Fig. 5 is about $2.5 - 3 \times 10^{-4}$. For features B and D, which we hypothesize to have (101) Burgers vectors, the projection onto the $(\bar{1}13)$ diffraction axis yields strain of about $1.1 - 1.3 \times 10^{-4}$ —below the minimum measurable strain. This result is consistent with our observations, where only the edges of features B and D are visible with $(\bar{1}13)$ diffraction.

Note that this minimum detectable value applies to compressive strain. A similar analysis applies to tensile strain, which will shift the diffraction peak toward smaller 2θ . For the CVD-diamond sample, tensile strain shifts the strain-feature-induced diffraction peak across the detector region dominated by the slowly varying overall line shape; the background-subtraction technique is therefore less sensitive to small tensile strain. Tensile strain at the level of approximately 2×10^{-3} would be needed for a feature to be detectable. In practice, we only observe compressively strained regions of growth defects in the 40- μm overgrowth layer in this sample. In general, the method presented here is applicable to both compressive and tensile strains, with the minimum measurable strain depending on the uniformity of the host crystal. However, a major advantage of our method is the ability to extract information even in the presence of a very inhomogeneous host crystal, as found in the CVD quantum sensing diamond.

(In Fig. 5, we do not measure features with submicron spatial scale in all dimensions, similar to those seen in Fig. 2; see the discussion in Sec. K of the Supplemental Material [24].)

III. THREE-DIMENSIONAL MODEL OF STRAIN-FEATURE GEOMETRY

High-spatial-resolution three-dimensional strain mapping within diamond samples is essential to the dark-matter detection proposal discussed in Sec. V. Additionally, three-dimensional high-resolution strain measurements enhance analysis of CVD-diamond growth and optical structure fabrication. By combining measurements at two diffraction angles with prior information about growth conditions and established knowledge of the structure of growth defects in CVD diamond, we generate a three-dimensional model of strain-feature geometry in this 24 000- μm^3 region of the CVD-diamond sample, as shown in Fig. 6. The construction of an assumption-free three-dimensional model using this method would require additional measurements at orthogonal Bragg conditions [34,35]; however, constraints on experimental geometry

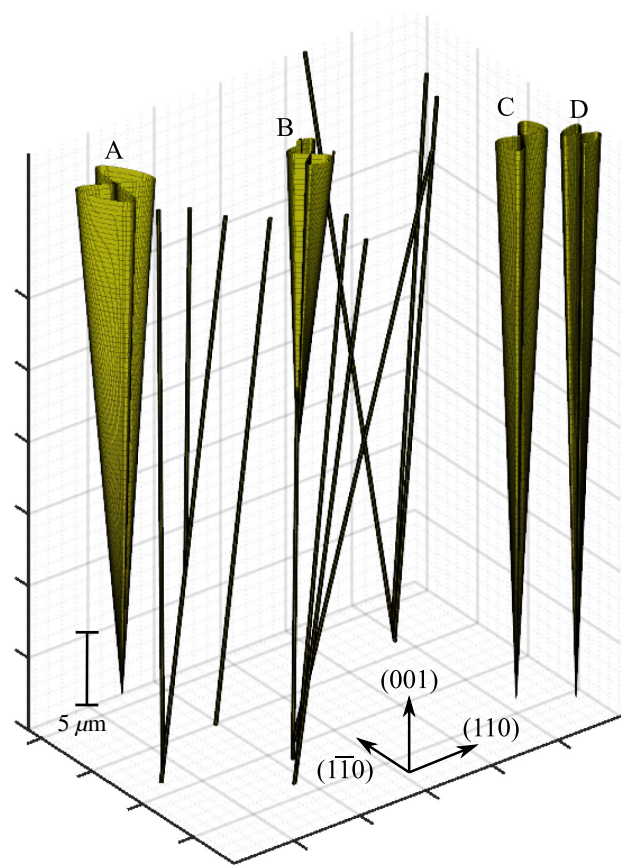


FIG. 6. The three-dimensional geometric model of compressively strained volumes in the region shown in Fig. 5, determined from two x-ray projections and constrained by crystal-growth assumptions and an associated model of the strain features (see text). The volumes indicated have strain above a threshold of 2×10^{-4} . The labeled regions correspond with the labels in Fig. 5. For a schematic illustration of the projection of similar features to create data such as those presented in Fig. 5, see Sec. I of the Supplemental Material [24]. For further discussion of the creation of the three-dimensional model from projected stereoscopic data, see Sec. K of the Supplemental Material [24].

during the current demonstration limit us to the nonorthogonal (113) and $(\bar{1}13)$ mirror planes. We constrain the model with two assumptions: first, that extended defects in CVD diamond generally nucleate at the interface with the substrate and propagate close to (but not perfectly along) the growth direction [32]; and, second, that the integrated strain far from a defect must converge to zero [36].

Two features types that satisfy these constraints and that have been widely observed in diamonds grown under similar conditions to our sample are bundles of linear edge or screw dislocations and “petal”- or “clover”-shaped extended defects [6,32,37,38]. We therefore build our three-dimensional model from such features, constrained by the diffraction measurements (for further discussion of these feature types, see Sec. J of the Supplemental Material [24]).

We first identify individual features in the projected strain maps and classify them as either “petals” or “rods.” We note that some of the “rods” likely represent the high-strain edges of “petal” features with small (113) or $(\bar{1}13)$ projections, as discussed in Sec. II; measurements at additional projection angles would be required to resolve this ambiguity. For each identified feature, we construct a corresponding entity in our three-dimensional model and constrain its geometrical parameters by minimizing the difference between the data and the model (for further details on constraining the parameters of the model, see Sec. L of the Supplemental Material [24]).

We finally note two nontrivial results obtained from this analysis. First, the strain features exhibit sharp distinct edges where they intersect the host crystal matrix; and, second, we observe smoothly varying but nonuniform strain within the features. While the construction of a full microscopic model of the strained regions is beyond the scope of this work, our data suggest that the crystal dislocations that comprise such clover-shaped features may be concentrated at or near the “petal” boundaries, enclosing a region of strained crystal, rather than evenly spread throughout the strained volume.

IV. COMPARISON WITH STRAIN MEASUREMENTS FROM THE QUANTUM DIAMOND MICROSCOPE

Optical methods for strain measurements in diamond are diffraction-limited in spatial resolution to a few hundred nanometers and are not in general sensitive to three-dimensional spatial structure. In particular, ensemble $N-V$ spectroscopy measures integrated stress throughout the nitrogen-doped layer [6]. Despite lower spatial resolution and two-dimensional projective imaging, optical strain or stress measurements via $N-V$ spin-state spectroscopy offer complementary advantages over SXDM. Wider fields of view enable fast location of regions of interest for high-resolution diffraction measurements, which is necessary for directional WIMP detection [22]. Additionally, such optical methods are capable of measuring strain as low as 10^{-6} , albeit only as an average over an optical pixel. Finally, from optical measurements it is possible to reconstruct the entire strain tensor [6], which could inform the choice of Bragg angles used for diffraction.

To illustrate the complementary application of x-ray and optical methods, we use a quantum diamond microscope (QDM) [1] to image the same field of view featured in our nanoprobe diffraction measurements of the CVD quantum sensing diamond. In a QDM, $N-V$ centers in diamond are excited with green laser light and their spin-state is controlled with applied microwaves; the spin state and environment of the nitrogen vacancies can then be determined. QDMs are commonly used to image dc magnetic fields but have also been used for sensitive stress and

strain measurements. The QDM results reported in this work are performed by determining the stress Hamiltonian from $N-V$ spin-state-dependent optical measurements. For an overview of QDM methods, see Sec. M of the Supplemental Material [24]; for full details of the technique and apparatus used, see Ref. [6]. The stress tensor is converted to strain using the measured elasticity tensor for diamond [39].

In the present work, QDM images are taken after the SXDM measurements; to find appropriate regions of interest to develop SXDM on diamond, we perform relatively time-consuming wide-area scans with the HXN. The future development of SXDM for diamond engineering and dark-matter detection will use QDM measurements to more extensively inform SXDM parameters.

Figures 7 and 8 compare the strain-feature geometrical model obtained from SXDM data and our methodology with QDM strain-tensor measurements. The QDM measurements demonstrate poorer spatial resolution ($1\text{--}10\ \mu\text{m}$), limited by the collection of light from the entire axial focal length of the microscope objective used. Nonetheless, these figures demonstrate good agreement between the two techniques with regard to the strain geometry over large length scales.

The QDM measurement distinguishes between tensile and shear strains, while SXDM measures a projection of both onto the diffracting crystal axes. For the comparison in Fig. 7, we therefore sum all strain-tensor elements measured using the QDM, to obtain a map of strain-feature positions regardless of orientation; we compare that map to

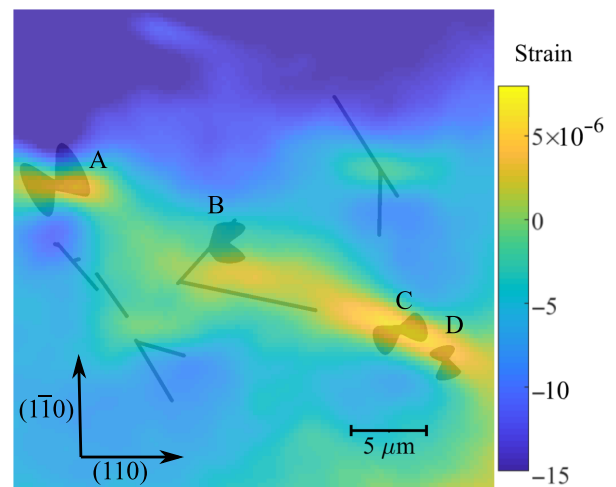


FIG. 7. The sum of the strain-tensor elements measured using a quantum diamond microscope (QDM), overlain with a vertical projection of a three-dimensional geometric model of strain features derived from SXDM measurements. The color map and the corresponding scale bar represent strain measured with QDM, while the wire-frame objects are the projected model. The labeled features correspond with the labels in Figs. 5 and 6.

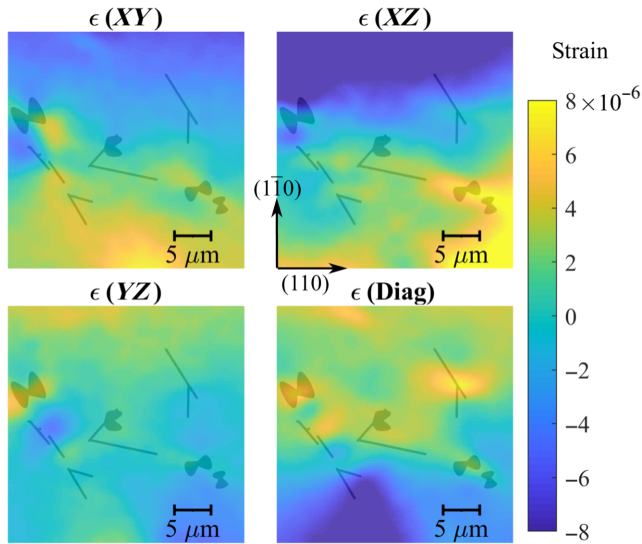


FIG. 8. A comparison between the QDM strain-tensor measurements and the three-dimensional geometric model of growth-defect regions from SXDM measurements. The strain-tensor elements ϵ_{ij} give strain on the i crystal plane in the j direction; $\epsilon(\text{Diag})$ is the normal strain, while the other tensor elements give shear strain. Constant offsets have been subtracted from QDM strain-tensor measurements to simplify comparison on common color scales.

the geometry obtained from SXDM data. In this comparison, the positions of the four “petal” features A, B, C, and D correspond to the three strongest strain features identifiable in the QDM data (features C and D are too close together for the QDM to resolve them individually). This agreement between the SXDM and QDM approaches validates the SXDM measurement of strain features via the reduced diffraction curve, as well as the three-dimensional model. Additionally, the “rod” positions agree relatively well with the remaining strain features in the QDM measurement. This supports the hypothesis that some or all “rods” may actually be high-strain edges of additional “petal” regions, at the centers of which the projection onto the (113) and $(\bar{1}13)$ axes is below the SXDM detection threshold.

Figure 8 compares individual elements of the strain tensor from QDM measurements with the geometrical model from SXDM measurements. Generically, a strain-tensor element ϵ_{ij} gives the change in the position of the i crystal plane along the j direction. For $i = j$, ϵ is the normal strain on the i planes, while for $i \neq j$ ϵ is the shear strain. The comparison in Fig. 8 shows the additional information that can be gained from performing both QDM and x-ray diffraction measurements on the same sample; note that several of the strain features come through much more strongly in some strain-tensor elements than in others, especially the lower-left “rod” features in $\epsilon(YZ)$ and the upper-right “rod” feature in $\epsilon(\text{Diag})$. The QDM thus

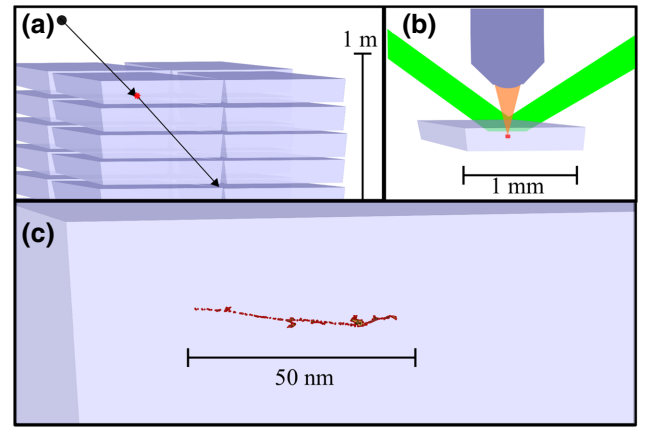


FIG. 9. The application of spatially resolved nanoscale strain measurement to dark-matter detection. (a) WIMP dark matter target interacts with a carbon nucleus in a sectioned diamond target, triggering detector elements. (b) The triggered section is removed from target and imaged or scanned; crystal damage due to nuclear recoils is localized to a micrometer-cubed voxel. (c) Within the diamond section, the orientation and asymmetry of the damage track and the resulting nanoscale strain preserve information about the incident direction of the WIMP. This information can be read out using the scanning x-ray nanodiffraction techniques presented here. The pictured feature is crystal-lattice damage from a nuclear recoil track following a 10-keV impact between a WIMP and a carbon nucleus, simulated using the SRIM software [18,40].

illuminates the direction of shear strains and gives information about strain on longer length scales, while the nanoprobe measurement gives higher spatial resolution and reveals the three-dimensional structure of the strain features.

We note that several other methods have been applied to optically measure strain in CVD diamond, although none fills the role of SXDM for high-resolution three-dimensional strain measurements. Optical birefringence measures strain integrated through the length of the crystal [9]. Bulk x-ray tomography has been applied to similar CVD diamonds: it provides three-dimensional images but suffers from lower spatial and strain resolution than SXDM [32]. Strain measurements using spectroscopy of single N-V centers are perhaps the most comparable to SXDM in terms of obtaining three-dimensional information [11]. However, the need to resolve individual N-V centers in the bulk of the diamond limits the spatial resolution approximately to the micron level and limits the application of the technique to diamonds with a narrow range of N-V densities.

V. TOWARD DARK-MATTER DETECTION

We finish by characterizing the performance of the SXDM strain mapping technique as applied to the CVD quantum sensing diamond in the context of the proposed

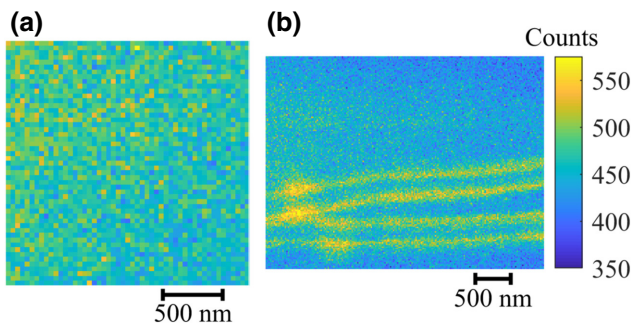


FIG. 10. SXDM scans of representative “background” regions in the CVD quantum sensing diamond, away from large-scale strain features, demonstrate the absence of preexisting features that could be mistaken for WIMP recoil tracks. Each plot shows the number of detector counts arising from compressively strained diamond in the CVD overgrowth layer—for details, see Sec. C of the Supplemental Material [24]. (Note that in these plots we do not apply the background subtraction and strain analysis described in Sec. II; instead, the total signal from any compressively strained diamond gives a better indication of the presence or absence of small or weak features.) (a) Despite an overall strain gradient, a 40-nm-increment scan of the nanoprobe does not find features with the approximately 100-nm length scale expected for WIMP tracks. (b) A scan of a different background region, this time with 20-nm increments, reveals extended dislocation bundles, which can be easily distinguished from WIMP recoil tracks by their length; again, no strain features are observed having ≤ 100 nm scale in all three dimensions.

directional WIMP detector (see Fig. 9) [18,22]). We can estimate the strain signal from a WIMP collision following Ref. [22] and compare to the sensitivity analysis of Sec. II. We scale the strain per crystal lattice vacancy by the number of vacancies created [18] and the r^{-3} distance scaling of strain due to point defects [36]. For a particle-scattering event imparting 10 keV to a carbon nucleus—the low end of the directional sensitivity range of a diamond detector [18]—the average strain within 30 nm of the resulting damage track will be approximately 1.8×10^{-4} . This would be detectable with the SXDM technique even with the imperfect highly inhomogeneous diamond sample used in this demonstration.

Figure 10 presents results from a background SXDM scan, taken in two arbitrarily chosen regions away from strain features large enough to appear in birefringence or QDM measurements. Figure 10(b) includes a group of extended linear defects with observed strain signals approximately 100 nm wide, demonstrating spatial resolution well below the optical diffraction limit. This matches the expected length scale of WIMP-induced damage tracks for much of the target energy range. The spatial resolution limit of the HXN is approximately 10 nm at the minimum focal size [26], which matches requirements for resolving WIMP signatures [22]. If required, higher-resolution x-ray

strain imaging is possible via advanced techniques such as Bragg projection ptychography [41–43].

In addition to an instrument and technique capable of measuring nanoscale damage tracks in diamond, the proposed WIMP directional-detection method requires production of CVD-diamond crystals without preexisting strain features that could be misidentified as damage tracks. The data in Fig. 10 represent an initial step toward demonstrating such samples; in high-resolution SXDM scans, we see no evidence of strain features with submicron extent in all three dimensions, as expected for WIMP-induced damage tracks. In Fig. 10(a), despite the presence of a broad overall gradient, we see no sharp features; and in Fig. 10(b), we observe features that are approximately 100 nm wide but microns in length. Although further background characterization will be required before production of a directional WIMP detector, these initial results support the expectation that after high-temperature annealing, defects in CVD diamond should be either pointlike or extended, without structure at intermediate length scales of approximately 100 nm in all three dimensions [7,37].

VI. CONCLUSION

We perform SXDM with high spatial and strain resolution on two diamond samples—an HPHT diamond sample with a relatively homogeneous crystal structure and a CVD-diamond sample featuring a 40- μm layer of dense N- V centers. Using a background-subtraction technique applied to SXDM diffraction curves, we measure the strain in small growth-defect volumes within the crystal matrix in both diamonds. In the HPHT diamond, we measure spatially small strain features, with length scales of order 100 nm, demonstrating the resolution and feature sensitivity achievable with SXDM. In the CVD diamond, we measure strain in micron-scale growth defects persisting throughout the 40- μm overgrowth layer, despite a broad inhomogeneous diffraction signal arising from the layered structure of the sample and its high impurity content. Such measurements will grant valuable insight into defect development and mitigation during diamond growth, with implications for future defect-based quantum sensing efforts, as well as for the development of diamond structure fabrication.

By combining measurements at two diffraction conditions, we create a geometrical model of several three-dimensional strained volumes in the CVD quantum sensing diamond. Subsequent stress measurements performed with N- V spin-state spectroscopy using a QDM show good agreement with this model, demonstrating the capability of SXDM to measure features that affect N- V sensing, as well as the complementary advantages of the two techniques. Their combination offers a window into the three-dimensional microscopic structure of strain features in diamond.

Finally, we evaluate the performance of the SXDM techniques for a proposed directional detector of WIMP dark matter. The HPHT-diamond results demonstrate the ability to measure features at the length scales expected for WIMP-induced nuclear recoil tracks. The strain sensitivity and three-dimensional resolution—characterized in the inhomogeneous layered CVD diamond—approach or exceed the requirements for WIMP detection. In an ideal detector segment—a homogeneous crystal without a substrate layer or mechanical polishing damage—the minimum detectable nanoscale strain with the SXDM method should be between 2 and 20 times smaller [25]. Additionally, a limited initial survey finds no preexisting backgrounds to impede a dark-matter search. Such a detector technology—with high target density and directional detection capability—would enable WIMP searches to push sensitivity below the neutrino floor, opening a path for future generations of WIMP detectors.

ACKNOWLEDGMENTS

We acknowledge useful discussions and feedback from Connor Hart and Reza Ebadi. This work was supported by the U.S. Department of Energy (DOE) “Quantum Information Science Enabled Discovery” (QuantISED) program under Award No. DE-SC0019396; the Army Research Laboratory Maryland-ARL Quantum Partnership (MAQP) program under Contract No. W911NF-19-2-0181; the Defense Advanced Research Projects Agency (DARPA) “Driven and Nonequilibrium Quantum Systems” (DRINQS) program under Grant No. D18AC00033; and the University of Maryland Quantum Technology Center. This work was performed in part at the Harvard Center for Nanoscale Systems (CNS), a member of the National Nanotechnology Coordinated Infrastructure Network (NNCI), which is supported by the National Science Foundation under NSF Award No. 1541959. Work at Argonne was supported by the Center for Novel Pathways to Quantum Coherence in Materials, an Energy Frontier Research Center funded by the U.S. Department of Energy, Office of Science, Basic Energy Sciences in collaboration with the U.S. Department of Energy, Office of Science, National Quantum Information Science Research Centers. The SXDM measurements were performed at the Hard X-ray Nanoprobe Beamline operated by the Center for Nanoscale Materials and the Advanced Photon Source, both Office of Science user facilities supported by the U.S. Department of Energy, Office of Science, Office of Basic Energy Sciences, under Contract No. DE-AC02-06CH11357.

[1] E. V. Levine, M. J. Turner, P. Kehayias, C. A. Hart, N. Langellier, R. Trubko, D. R. Glenn, R. R. Fu, and R.

- L. Walsworth, Principles and techniques of the quantum diamond microscope, *Nanophotonics* **8**, 1945 (2019).
- [2] R. Schirhagl, K. Chang, M. Lorez, and C. L. Degen, Nitrogen-vacancy centers in diamond: Nanoscale sensors for physics and biology, *Annu. Rev. Phys. Chem.* **65**, 83 (2014).
- [3] A. Boretti, L. Rosa, J. Blackledge, and S. Castelletto, Nitrogen-vacancy centers in diamond for nanoscale magnetic resonance imaging applications, *Beilstein J. Nanotechnol.* **10**, 2128 (2019).
- [4] J. M. Taylor, P. Cappellaro, L. Childress, L. Jiang, D. Budker, P. R. Hemmer, A. Yacoby, R. Walsworth, and M. D. Lukin, High-sensitivity diamond magnetometer with nanoscale resolution, *Nat. Phys.* **4**, 810 (2008).
- [5] G. Balasubramanian, I. Y. Chan, R. Kolesov, M. Al-Hmoud, J. Tisler, C. Shin, C. Kim, A. Wojcik, P. R. Hemmer, A. Krueger, T. Hanke, A. Leitenstorfer, R. Bratschkitsch, F. Jelezko, and J. Wrachtrup, Nanoscale imaging magnetometry with diamond spins under ambient conditions, *Nature* **455**, 648 (2008).
- [6] P. Kehayias, M. J. Turner, R. Trubko, J. M. Schloss, C. A. Hart, M. Wesson, D. R. Glenn, and R. L. Walsworth, Imaging crystal stress in diamond using ensembles of nitrogen-vacancy centers, *Phys. Rev. B* **100**, 174103 (2019).
- [7] I. Friel, S. L. Clewes, H. K. Dhillon, N. Perkins, D. J. Twitchen, and G. A. Scarsbrook, Control of surface and bulk crystalline quality in single crystal diamond grown by chemical vapour deposition, *Diamond Relat. Mater. Proc. Diamond 2008, the 19th Eur. Conf. Diamond, Diamond-Like Mater., Carbon Nanotubes, Nitrides and Silicon Carbide* **18**, 808 (2009).
- [8] A. M. Edmonds, C. A. Hart, M. J. Turner, P.-O. Colard, J. M. Schloss, K. Olsson, R. Trubko, M. L. Markham, A. Rathmill, B. Horne-Smith, W. Lew, A. Manickam, S. Bruce, P. G. Kaup, J. C. Russo, M. J. DiMario, J. T. South, J. T. Hansen, D. J. Twitchen, and R. L. Walsworth, Characterisation of CVD diamond with high concentrations of nitrogen for magnetic-field sensing applications, *Mater. Quantum Technol.* **1**, 025001 (2021).
- [9] L. T. M. Hoa, T. Ouisse, D. Chaussende, M. Naamoun, A. Tallaire, and J. Achard, Birefringence microscopy of unit dislocations in diamond, *Cryst. Growth. Des.* **14**, 5761 (2014).
- [10] D. Broadway, B. Johnson, M. Barson, S. Lillie, N. Dentschuk, D. McCloskey, A. Tsai, T. Teraji, D. Simpson, A. Stacey, J. McCallum, J. Bradby, M. Doherty, L. Hollenberg, and J.-P. Tetienne, Microscopic imaging of the stress tensor in diamond using *in situ* quantum sensors, *Nano Lett.* **19**, 4543 (2019).
- [11] M. E. Trusheim and D. Englund, Wide-field strain imaging with preferentially aligned nitrogen-vacancy centers in polycrystalline diamond, *New J. Phys.* **18**, 123023 (2016).
- [12] M. Schreck, P. Ščajev, M. Trüger, M. Mayr, T. Grünwald, M. Fischer, and S. Gsell, Charge carrier trapping by dislocations in single crystal diamond, *J. Appl. Phys.* **127**, 125102 (2020).
- [13] X.-D. Chen, L.-M. Zhou, C.-L. Zou, C.-C. Li, Y. Dong, F.-W. Sun, and G.-C. Guo, Spin depolarization effect induced by charge state conversion of nitrogen vacancy center in diamond, *Phys. Rev. B* **92**, 104301 (2015).

- [14] J. Choi, S. Choi, G. Kucsko, P. C. Maurer, B. J. Shields, H. Sumiya, S. Onoda, J. Isoya, E. Demler, F. Jelezko, N. Y. Yao, and M. D. Lukin, Depolarization Dynamics in a Strongly Interacting Solid-State Spin Ensemble, *Phys. Rev. Lett.* **118**, 093601 (2017).
- [15] A. Sipahigil, R. E. Evans, D. D. Sukachev, M. J. Burek, J. Borregaard, M. K. Bhaskar, C. T. Nguyen, J. L. Pacheco, H. A. Atikian, C. Meuwly, R. M. Camacho, F. Jelezko, E. Bielejec, H. Park, M. Lončar, and M. D. Lukin, An integrated diamond nanophotonics platform for quantum-optical networks, *Science* **354**, 847 (2016).
- [16] B. J. M. Hausmann, B. J. Shields, Q. Quan, Y. Chu, N. P. de Leon, R. Evans, M. J. Burek, A. S. Zibrov, M. Markham, D. J. Twitchen, H. Park, M. D. Lukin, and M. Lončar, Coupling of NV centers to photonic crystal nanobeams in diamond, *Nano Lett.* **13**, 5791 (2013).
- [17] S. Knauer, J. P. Hadden, and J. G. Rarity, *In-situ* measurements of fabrication induced strain in diamond photonic-structures using intrinsic colour centres, *npj Quantum Inf.* **6**, 1 (2020).
- [18] S. Rajendran, N. Zobrist, A. O. Sushkov, R. Walsworth, and M. Lukin, A method for directional detection of dark matter using spectroscopy of crystal defects, *Phys. Rev. D* **96**, 035009 (2017).
- [19] N. Kurinsky, T. C. Yu, Y. Hochberg, and B. Cabrera, Diamond detectors for direct detection of sub-GeV dark matter, *Phys. Rev. D* **99**, 123005 (2019).
- [20] C. A. O'Hare, A. M. Green, J. Billard, E. Figueroa-Feliciano, and L. E. Strigari, Readout strategies for directional dark matter detection beyond the neutrino background, *Phys. Rev. D* **92**, 063518 (2015).
- [21] C. Bøehm, D. G. Cerdeño, P. A. N. Machado, A. O.-D. Campo, and E. Reid, How high is the neutrino floor?, *J. Cosmol. Astroparticle Phys.* **21**, 043 (2019).
- [22] M. C. Marshall, M. J. Turner, M. J.-H. Ku, D. F. Phillips, and R. L. Walsworth, Directional detection of dark matter with diamond, *Quantum Sci. Technol.* **6**, 024011 (2021).
- [23] R. Winarski, M. Holt, V. Rose, P. Fuesz, D. Carbaugh, C. Benson, D. Shu, D. Kline, G. Stephenson, I. McNulty, and J. Maser, A hard x-ray nanoprobe beamline for nanoscale microscopy, *J. Synchrotron Radiat.* **19**, 1056 (2012).
- [24] See the Supplemental Material at <http://link.aps.org/supplemental/10.1103/PhysRevApplied.16.054032>, which includes Refs. [44–50]. It includes additional details on the samples and analysis methods used, as referenced throughout the text.
- [25] M. Holt, R. Harder, R. Winarski, and V. Rose, Nanoscale hard x-ray microscopy methods for materials studies, *Annu. Rev. Mater. Res.* **43**, 183 (2013).
- [26] I. Mohacsi, I. Vartiainen, B. Rösner, M. Guizar-Sicairos, V. A. Guzenko, I. McNulty, R. Winarski, M. V. Holt, and C. David, Interlaced zone plate optics for hard x-ray imaging in the 10 nm range, *Sci. Rep.* **7**, 43624 (2017).
- [27] B. E. Warren, *X-Ray Diffraction* (Courier Corporation, New York, 1990), google-Books-ID: wflBhAbEYASc.
- [28] A. Ying, B. Osting, I. C. Noyan, C. E. Murray, M. Holt, and J. Maser, Modeling of kinematic diffraction from a thin silicon film illuminated by a coherent, focused x-ray nanobeam, *J. Appl. Crystallogr.* **43**, 587 (2010).
- [29] A. Pateras, J. Park, Y. Ahn, J. A. Tilka, M. V. Holt, H. Kim, L. J. Mawst, and P. G. Evans, Dynamical scattering in coherent hard x-ray nanobeam Bragg diffraction, *Phys. Rev. B* **97**, 235414 (2018).
- [30] J. A. Tilka, J. Park, Y. Ahn, A. Pateras, K. C. Sampson, D. E. Savage, J. R. Prance, C. B. Simmons, S. N. Coppersmith, M. A. Eriksson, M. G. Lagally, M. V. Holt, and P. G. Evans, Combining experiment and optical simulation in coherent x-ray nanobeam characterization of Si/SiGe semiconductor heterostructures, *J. Appl. Phys.* **120**, 015304 (2016).
- [31] B. W. Batterman and H. Cole, Dynamical diffraction of x rays by perfect crystals, *Rev. Mod. Phys.* **36**, 681 (1964).
- [32] M. P. Gaukroger, P. M. Martineau, M. J. Crowder, I. Friel, S. D. Williams, and D. J. Twitchen, X-ray topography studies of dislocations in single crystal CVD diamond, *Diam. Relat. Mater.* **17**, 262 (2008).
- [33] H. Pinto and R. Jones, Theory of the birefringence due to dislocations in single crystal CVD diamond, *J. Phys.: Condens. Matter* **21**, 364220 (2009).
- [34] F. Hofmann, E. Tarleton, R. J. Harder, N. W. Phillips, P.-W. Ma, J. N. Clark, I. K. Robinson, B. Abbey, W. Liu, and C. E. Beck, 3D lattice distortions and defect structures in ion-implanted nano-crystals, *Sci. Rep.* **7**, 45993 (2017).
- [35] F. Hofmann, N. W. Phillips, S. Das, P. Karamched, G. M. Hughes, J. O. Douglas, W. Cha, and W. Liu, Nanoscale imaging of the full strain tensor of specific dislocations extracted from a bulk sample, *Phys. Rev. Mater.* **4**, 013801 (2020).
- [36] J. D. Eshelby, Distortion of a crystal by point imperfections, *J. Appl. Phys.* **25**, 255 (1954).
- [37] H. Pinto, R. Jones, J. P. Goss, and P. R. Briddon, Point and extended defects in chemical vapour deposited diamond, *J. Phys.: Conf. Ser.* **281**, 012023 (2011).
- [38] A. Crisci, F. Baillet, M. Mermoux, G. Bogdan, M. Nesládek, and K. Haenen, Residual strain around grown-in defects in CVD diamond single crystals: A 2D and 3D Raman imaging study, *Phys. Status Solidi (a)* **208**, 2038 (2011).
- [39] C. A. Klein and G. F. Cardinale, in *Diamond Optics V*, Vol. 1759 (International Society for Optics and Photonics, 1992), p. 178.
- [40] J. F. Ziegler, M. D. Ziegler, and J. P. Biersack, SRIM—the stopping and range of ions in matter (2010), *Nucl. Instrum. Methods Phys. Res. Sec. B: Beam Interact. Mater. At. 19th Int. Conf. Ion Beam Anal.* **268**, 1818 (2010).
- [41] F. Pfeiffer, X-ray ptychography, *Nat. Photonics* **12**, 9 (2018).
- [42] S. O. Hruszkewycz, M. Allain, M. V. Holt, C. E. Murray, J. R. Holt, P. H. Fuoss, and V. Chamard, High-resolution three-dimensional structural microscopy by single-angle Bragg ptychography, *Nat. Mater.* **16**, 244 (2017).
- [43] M. Hill, I. Calvo-Almazan, M. Allain, M. Holt, A. Ulvestad, J. Treu, G. Koblmüller, C. Huang, X. Huang, H. Yan, E. Nazaretski, Y. Chu, G. Stephenson, V. Chamard, L. Lauhon, and S. Hruszkewycz, Measuring three-dimensional strain and structural defects in a single InGaAs nanowire using coherent x-ray multiangle Bragg projection ptychography, *Nano Lett.* **18**, 811 (2018).
- [44] M. J. Turner, N. Langellier, R. Bainbridge, D. Walters, S. Meesala, T. M. Babinec, P. Kehayias, A. Yacoby, E. Hu, M.

- Lončar, R. L. Walsworth, and E. V. Levine, Magnetic Field Fingerprinting of Integrated-Circuit Activity with a Quantum Diamond Microscope, *Phys. Rev. Appl.* **14**, 014097 (2020).
- [45] H. Pernegger, S. Roe, P. Weilhammer, V. Eremin, H. Fraiss-Kölbl, E. Griesmayer, H. Kagan, S. Schnetzer, R. Stone, W. Trischuk, D. Twitchen, and A. Whitehead, Charge-carrier properties in synthetic single-crystal diamond measured with the transient-current technique, *J. Appl. Phys.* **97**, 073704 (2005).
- [46] M. Gabrysch, *et al.*, Formation of secondary electron cascades in single-crystalline plasma-deposited diamond upon exposure to femtosecond x-ray pulses, *J. Appl. Phys.* **103**, 064909 (2008).
- [47] H. Jayakumar, J. Henshaw, S. Dhomkar, D. Pagliero, A. Laraoui, N. B. Manson, R. Albu, M. W. Doherty, and C. A. Meriles, Optical patterning of trapped charge in nitrogen-doped diamond, *Nat. Commun.* **7**, 12660 (2016).
- [48] G. Balasubramanian, P. Neumann, D. Twitchen, M. Markham, R. Kolesov, N. Mizuochi, J. Isoya, J. Achard, J. Beck, J. Tissler, V. Jacques, P. R. Hemmer, F. Jelezko, and J. Wrachtrup, Ultralong spin coherence time in isotopically engineered diamond, *Nat. Mater.* **8**, 383 (2009).
- [49] K. Gardner, E. Mueller, J. Tilka, and P. Evans, X-ray nanobeam dynamical diffraction simulator, <https://xray.engr.wisc.edu/nanobeamsimulation/dynamicalhtml/index.php>, accessed: 2020-09-09.
- [50] N. Tsubouchi and Y. Mokuno, Configuration of a single grown-in dislocation corresponding to one etch pit formed on the surface of CVD homoepitaxial diamond, *J. Cryst. Growth* **455**, 71 (2016).